

# Machine-Learned Invertible Coarse Graining for Multiscale Molecular Modeling

Jun Zhang<sup>1,†</sup>, Xiaohan Lin<sup>2</sup>, Weinan E<sup>3,4</sup> and Yi Qin Gao<sup>1,2</sup>

<sup>1</sup> Changping Laboratory, Beijing 102200, China

<sup>2</sup> Beijing National Laboratory for Molecular Sciences, College of Chemistry and Molecular Engineering, Peking University, Beijing 100871, China

<sup>3</sup> AI for Science Institute, Beijing, China

<sup>4</sup> Center for Machine Learning Research and School of Mathematical Sciences, Peking University, Beijing 100871, China

Correspondence should be sent to: † jzhang@cpl.ac.cn (Jun Zhang)

## Abstract

Multiscale molecular modeling is widely applied in scientific research of molecular properties over large time and length scales. Two specific challenges are commonly present in multiscale modeling, provided that information between the coarse and fine representations of molecules needs to be properly exchanged: One is to construct coarse grained (CG) models by passing information from the fine to coarse levels; the other is to restore finer molecular details given CG configurations. Although these two problems are commonly addressed independently, in this work, we present a theory connecting them, and develop a methodology called Cycle Coarse Graining (CCG) to solve both problems in a unified manner. In CCG, reconstruction can be achieved via a tractable optimization process, leading to a general method to retrieve fine details from CG simulations, which in turn, delivers a new solution to the CG problem, yielding an efficient way to calculate free energies in a rare-event-free manner. CCG thus provides a systematic way for multiscale molecular modeling, where the finer details of CG simulations can be efficiently retrieved, and the CG models can be improved consistently.

## I. INTRODUCTION

Multiscale modeling is critical in various fields of scientific research including physics, chemistry, biology, materials and engineering. For many-particle Hamiltonian systems, coarse-graining of the microscopic model can drastically simplify the representation of the physical system. Specifically, in molecular simulations [1] interactions between particles are described by the potential energy  $U(\mathbf{R})$  which is a function of the positions of particles (denoted by  $\mathbf{R}$ ). Since  $\mathbf{R}$  can be very high dimensional, the corresponding energy landscape  $U(\mathbf{R})$  is usually rugged with many local traps. As a result, fine grained (FG) or first-principle based simulations, including all-atom and *ab initio* molecular dynamics (MD), are known to suffer from limited accessible time and length scales.

One solution against this issue is to extract slowly changing CG variables of the system  $\mathbf{s} = s(\mathbf{R})$ , and build CG models accordingly. For example, in a widely used linear coarse graining protocol, groups of atoms or particles from a fine-grained model are bundled into single beads [2,3], thus eliminating the microscopic degrees of freedom (DoFs) that are not essential to resolve structural features above a certain length scale. CG variables can also be non-linear functions of  $\mathbf{R}$ , which are more often termed as collective variables [4-

6] and widely investigated in the context of enhanced sampling [7-9].

In molecular simulations, the CG potential  $F(\mathbf{s})$  should satisfy the *thermodynamic consistency principle* (Eqs. (1-2)), which states that  $F(\mathbf{s})$  should reproduce the marginalized Boltzmann distribution of the CG variables  $\mathbf{s}$  given the FG potential  $U(\mathbf{R})$ ,

$$p(\mathbf{s}) = \frac{\int e^{-\beta U(\mathbf{R})} \delta(\mathbf{s} - s(\mathbf{R})) d\mathbf{R}}{\int e^{-\beta U(\mathbf{R})} d\mathbf{R}} \quad (1)$$
$$= \frac{e^{-\beta F(\mathbf{s})}}{Z}$$

$$F(\mathbf{s}) = -\frac{1}{\beta} [\log p(\mathbf{s}) + \log Z] \quad (2)$$

where  $\beta$  is the inverse temperature,  $\delta$  denotes the Dirac-delta function and  $Z = \int e^{-\beta U(\mathbf{R})} d\mathbf{R}$  is the partition function.

Under this setting, the CG potential  $F(\mathbf{s})$  becomes a simplified description of the original thermodynamic system and is usually much smoother than the original energy landscape  $U(\mathbf{R})$ . Consequently, CG simulations performed under  $F(\mathbf{s})$  are generally much faster, hence, can reach larger time and length scales that are inaccessible to the fine-

grained models [3], despite that the finer details of the system are lost. Various approaches have been developed to parametrize CG models satisfying Eqs. (1-2), such as Iterative Boltzmann inversion [10], force matching [11], and relative entropy [12], etc. Some recent improvement along this line includes the deployment of artificial neural networks to augment the expressivity and complexity of the CG potentials [13,14], as well as the use of generative and reinforcement learning to boost the training efficiency of CG models in lack of FG simulation samples [15,16].

However, in many applications, one may need to simulate large systems with long correlation time in sufficiently fine details. Examples include the studies of the interaction between biological macromolecules [17], and the local structure of polymers at the interface with solid surfaces [18], etc. In these cases, a reconstruction approach, which will be referred to as *fine-grained reconstruction* (FGR) hereafter, is needed in order to retrieve or reconstruct reasonable FG structures consistent with the given CG model, and it has been noted that reconstruction is an integral part for systematical multiscale modeling [19]. Unfortunately, FGR has not been as well studied as CG, partly due to the ill-posed definition of FGR provided that mathematically  $s(\mathbf{R})$  is usually a non-invertible function. In other words, for a given CG rule  $s(\mathbf{R})$ , there exists one unique way to map one FG structure  $\mathbf{R}$  into one CG structure  $\mathbf{s}$ . In contrast, many different FG configurations can be assigned to the same CG structure, and it usually remains *ad hoc* to choose the “correct” one. Due to this difficulty, existing FGR methods, such as random mapping and position-restrained molecular dynamics (MD), commonly rely on system-specific knowledge and manually engineered fragment libraries [20-23], hence, are limited in scopes and lack of generalizability. Worse still, in most studies, CG and FGR problems were treated in a disconnected manner, and there lacks a unified theory to establish the relation between these two deeply coupled problems.

In this work, we formally formulate FGR as a probabilistic learning problem, and demonstrate that the FGR problem can be systematically solved by means of machine learning as an optimization problem. Moreover, we also draw a mathematical relation between the CG and FGR problems, and develop Cycle Coarse Graining (CCG), a general-purpose approach to performing multiscale modeling for molecular simulations: Based on machine learning, CCG delivers a tractable solution to the FGR problem. In turn, it also provides a rare-event-free way to perform coarse graining or calculate free energies, and allows efficient equilibrium sampling of rare events governed by the CG variables.

## II. METHODS

### 1. Fine-grained reconstruction with thermodynamic consistency

In molecular simulations, given the coarse-graining function  $s(\mathbf{R})$ , any FG structure  $\mathbf{R}$  that satisfies  $s(\mathbf{R}) = \mathbf{s}$  can be considered as a valid reconstruction for the given CG structure  $\mathbf{s}$ . The distribution of all such valid reconstructions can be written in the form of a conditional probability (Eq. (3)),

$$\mathbf{R} \sim p(\mathbf{R}; \mathbf{s}) \quad (3)$$

Equation (3) provides a general statistical viewpoint to the FGR problem, and existing FGR methods can be categorized according to how they choose and sample from  $p(\mathbf{R}; \mathbf{s})$ . We then formally decompose the FGR problem into two sub-problems: i) defining a reasonable reconstruction distribution  $p(\mathbf{R}; \mathbf{s})$ , and ii) efficiently drawing samples from  $p(\mathbf{R}; \mathbf{s})$ .

For the first task, a natural selection of  $p(\mathbf{R}; \mathbf{s})$  is given by Eq. (4),

$$p(\mathbf{R}; \mathbf{s}) = \frac{e^{-\beta U(\mathbf{R})} \delta(\mathbf{s} - s(\mathbf{R}))}{Z(\mathbf{s})} \quad (4)$$

where  $Z(\mathbf{s}) = \exp(-\beta F(\mathbf{s}))$  is the marginal partition function given a reference  $\mathbf{s}$ . In terms of physics,  $p(\mathbf{R}; \mathbf{s})$  defined in Eq. (4) allows a CG structure to be reconstructed into thermodynamically favourable FG structures according to the Boltzmann distribution. We thus name Eq. (4) as the *thermodynamic consistency principle* for FGR, in analogy with the thermodynamic consistency principle for CG (Eqs. (1-2)).

The remaining task is to draw samples according to Eq. (4). Conventionally, this is done by restrained or targeted MD [6,24]. However, after applying the restraints (typically in harmonic forms), computing the partition function in Eq. (4) becomes intractable. Alternatively, sampling according to Eq. (4) can be translated as a conditional generative learning problem, which has been intensively investigated by the machine learning community over topics like image super-resolution [25,26]. Therefore, we may turn the sampling problem into a more tractable optimization task and employ proper deep learning techniques to achieve this goal [27].

### 2. Deep generative learning for fine-grained reconstruction

In line with deep generative learning such as generative adversarial networks (GAN) [28], we start with a “generator”, e.g., a neural network model parametrized by  $\theta$  which generates samples  $\mathbf{R}$  according to an optimizable generative distribution  $q_\theta(\mathbf{R}; \mathbf{s})$ . Usually sampling from  $q_\theta(\mathbf{R}; \mathbf{s})$  is done via the re-parametrization trick [28,29]:

$$\begin{aligned} \mathbf{R} &= f_\theta(\mathbf{z}; \mathbf{s}) \Leftrightarrow \mathbf{R} \sim q_\theta(\mathbf{R}; \mathbf{s}) \\ q_\theta(\mathbf{R}; \mathbf{s}) &:= \int \delta(f_\theta(\mathbf{z}; \mathbf{s}) - \mathbf{R}) p(\mathbf{z}) d\mathbf{z} \end{aligned} \quad (5)$$

where  $f_\theta$  is a function transforming a random variable  $\mathbf{z}$  into a configuration sample  $\mathbf{R}$ , and  $\mathbf{z}$  usually comes from a tractable prior distribution (or base distribution) like standard normal.

We then aim to tune the model parameters  $\theta$  so that the resulting  $q_\theta$  is identical or close enough to the target reconstruction distribution  $p(\mathbf{R}; \mathbf{s})$  defined in Eq. (4). To achieve this goal, we can minimize a strict divergence, for example, Kullback-Leibler divergence  $D_{\text{KL}}$  (Eq. (S1); see SI for more details), between the generative distribution and the reconstruction distribution.

As in variational inference [30],  $q_\theta$  can be optimized by minimizing  $D_{\text{KL}}(q_\theta(\mathbf{R}; \mathbf{s}) || p(\mathbf{R}; \mathbf{s}))$  following the gradient in Eq. (5):

$$\nabla_\theta D_{\text{KL}}(q_\theta || p) = \mathbb{E}_{\mathbf{R} \sim q_\theta} [\nabla_\theta \log q_\theta(\mathbf{R}; \mathbf{s}) + \beta \nabla_\theta U(\mathbf{R}; \mathbf{s})] \quad (5)$$

Note that computing this gradient can be done without calculating the partition function  $Z(\mathbf{s})$ , thus forgoing sampling from  $U(\mathbf{R})$ . Given access to a potential energy function  $U(\mathbf{R})$  such as a force field, optimization of Eq. (5) can be done without data, so we call Eq. (5) the *energy-based* training objective (see more details in SI).

On the other hand, if samples  $\{\mathbf{R}_i\}_{i=1, \dots, N}$  are drawn via FG simulations, yielding a paired dataset  $\mathcal{D} = \{(\mathbf{R}_i; s(\mathbf{R}_i))\}$ , we can also minimize the reversed KL divergence  $D_{\text{KL}}(p(\mathbf{R}; \mathbf{s}) || q_\theta(\mathbf{R}; \mathbf{s}))$ , which is called the *data-based* training objective and equivalent to maximum likelihood estimation (MLE), to optimize the generative distribution:

$$\begin{aligned} \nabla_\theta D_{\text{KL}}(p || q_\theta) &= \mathbb{E}_{\mathbf{R} \sim p} [-\nabla_\theta \log q_\theta(\mathbf{R}; \mathbf{s})] \\ &\approx \mathbb{E}_{\mathbf{R} \in \mathcal{D}} [-\nabla_\theta \log q_\theta(\mathbf{R}; \mathbf{s})] \end{aligned} \quad (6)$$

In order to optimize  $q_\theta$  according to either of the two objectives or both (Eq. (S5) in SI), we need to conveniently draw samples from  $q_\theta$  and express  $\log q_\theta$  in a closed form. Both issues can be solved if  $q_\theta$  is parametrized by a deep bijective or invertible model (such as the normalizing-flow models in machine learning literature) and make use of the *change-of-variable* formula [31]. Specifically, given a function  $f_\theta$  that maps a random variable  $\mathbf{z}$  *bijectively* to  $\mathbf{R}$  given an  $\mathbf{s}$ , i.e.,  $\mathbf{R} = f_\theta(\mathbf{z}; \mathbf{s})$ , and assuming that  $\mathbf{z}$  comes from a tractable Gaussian base distribution  $q(\mathbf{z}; \mathbf{s})$  conditioned on  $\mathbf{s}$ , we can then define a complex distribution  $q_\theta(\mathbf{R}; \mathbf{s})$  so that the sampling from this distribution remains straightforward according to Eq. (7),

$$\log q_\theta(\mathbf{R}; \mathbf{s}) = \log q(\mathbf{z}; \mathbf{s}) - \log \left| \det \left( \frac{\partial f_\theta}{\partial \mathbf{z}} \right) \right| \quad (7)$$

where  $\det(\partial f / \partial \mathbf{z})$  is the determinant of the Jacobian matrix  $\partial f / \partial \mathbf{z}$ . In addition to bijective models, various approximations for the likelihood in Eq. (6) exist in literature, and they can be used for data-based training as well [29,32].

The remaining issue is how to impose the constraint  $s(\mathbf{R}) = \mathbf{s}$  when optimizing  $q_\theta$  (or  $f_\theta$ ). If  $s(\mathbf{R})$  is a linear function, as in most particle-based CG models [2,33], the constraint can be rigorously preserved by means of substitution of variables. While in a more general case where  $s(\mathbf{R})$  is non-linear, we can approximate  $\delta(\mathbf{s} - s(\mathbf{R}))$  in Eq.

(4) using smooth functions, although Lagrangian methods [34,35] can also be used. Taking energy-based training as example, when a Gaussian kernel is used to approximate the Dirac  $\delta$  function, the gradient of the loss function becomes,

$$\mathbb{E}_{\mathbf{R} \sim q_\theta} \left[ \nabla_\theta \log q_\theta(\mathbf{R}; \mathbf{s}) + \beta \nabla_\theta U(\mathbf{R}; \mathbf{s}) + \lambda \nabla_\theta \| \mathbf{s} - s(\mathbf{R}; \mathbf{s}) \|^2 \right] \quad (8)$$

where  $\lambda$  characterizes the bandwidth of the Gaussian kernel. In this way the constraint is relaxed into a restraint, and the hyper-parameter  $\lambda$  can be regarded as a regularization factor which is reminiscent of the force constant defining a harmonic restraint potential applied in the restrained MD simulations. We call this restraint term *consistency regularization* or *cycle loss*, and remark that it has other interpretations in related machine learning literature. For example, a similar term is incorporated by Cycle-GAN for unsupervised image-to-image translation [36], and used for mutual information maximization which helps overcome the mode-dropping issue in the studies of GANs [37].

### 3. Cycle coarse graining

An important relation can be drawn between CG and FGR on the basis of the two thermodynamic consistency principles, namely, Eq. (1) and Eq. (4). Given a deterministic CG rule  $s(\mathbf{R})$ , the Boltzmann distribution of the FG potential  $U(\mathbf{R})$  can be factorized in the form of Eq. (9),

$$\begin{aligned} p(\mathbf{R}) &= \frac{e^{-\beta U(\mathbf{R})}}{Z} \\ &= p(\mathbf{R}, s(\mathbf{R})) = \int p(\mathbf{s}) \cdot p(\mathbf{R}; \mathbf{s}) d\mathbf{s} \end{aligned} \quad (9)$$

where  $p(\mathbf{R}, s(\mathbf{R}))$  denotes the joint distribution of  $\mathbf{R}$  and  $s(\mathbf{R})$ ,  $p(\mathbf{s})$  is given by Eq. (1) and  $p(\mathbf{R}; \mathbf{s})$  by Eq. (4), respectively. Equation (9) shows that, to investigate the equilibrium properties of the FG model, instead of directly sampling from  $p(\mathbf{R})$  which is typically time-consuming, one can perform *factorized sampling*: First sample at a coarse-grained scale according to  $p(\mathbf{s})$ , then perform FGR according to  $p(\mathbf{R}; \mathbf{s})$  and retrieve finer details. Factorized sampling thus corresponds to a general multi-scale sampling approach. Intuitively, Eq. (9) would not hold unless that the motions of CG variable  $s(\mathbf{R})$  can be decoupled with other DoFs, echoing the common practice that only the most slowly-varying DoFs shall be chosen as CG variables. One intriguing advantage of factorized sampling lies in its ability to “interpolate” or “extrapolate” along the CG variables. Consider that  $s(\mathbf{R})$  is a characteristic chemical reaction coordinate, Eq. (9) then allows us to explore the reaction

coordinate in a rare-event-free manner, and can be further boosted by existing enhanced sampling methods [38-41]. Although such interpolated trajectories can do not necessarily correspond to the true reaction pathways, however, many approaches can be implemented to retrieve the correct kinetics or transition pathways given the reconstructed free energy profile [42,43].

Finally, we notice that solving the FGR problem defined in Eq. (4) simultaneously yields a novel solution to the CG problem in Eq. (1). Specifically, given a bijective generator  $f_\theta(\mathbf{z}; \mathbf{s})$  corresponding to a generative distribution  $q_\theta(\mathbf{R}; \mathbf{s})$  (Eq. (7)) which minimizes  $D_{\text{KL}}(q_\theta||p)$  or  $D_{\text{KL}}(p||q_\theta)$ , the *variational free energy*  $F_\theta(\mathbf{s})$  in the form of Eq. (10) is a good approximation to the ground-truth free energy  $F(\mathbf{s})$  in Eq. (2),

$$-\log p_\theta(\mathbf{s}) := \beta F_\theta(\mathbf{s}) \quad (10)$$

$$\beta F_\theta(\mathbf{s}) = \mathbb{E}_{\mathbf{z} \sim p(\mathbf{z}|\mathbf{s})} [\log q_\theta(f_\theta(\mathbf{z}; \mathbf{s})) + \beta U(f_\theta(\mathbf{z}; \mathbf{s}))]$$

where  $F_\theta(\mathbf{s})$  is an upper bound to  $F(\mathbf{s})$  (see Supplemental Texts in SI for derivation of Eq. (10)). As a result, we can approximate the free energy or construct CG potential function of  $\mathbf{s}$  through an optimized FGR generator  $f_\theta$  according to Eq. (10). The assembled training and inference protocol of CCG is summarized in SI and Algorithm S1.

In summary, by solving the FGR problem, we can obtain a generative model  $q_\theta(\mathbf{R}; \mathbf{s})$  or  $f_\theta(\mathbf{z}; \mathbf{s})$  which reconstructs FG structures according to the CG variables (Eq. (4)). On the other hand, the optimized FGR model  $q_\theta$  in turn gives rise to a CG potential  $F_\theta(\mathbf{s})$  (Eq. (10)), without calculating the mean forces or sampling the rare events explicitly. Finally, combining  $F_\theta$  and  $q_\theta$ , we can perform efficient multiscale sampling over a complex  $U(\mathbf{R})$  in a factorized fashion (Eq. (9)). This workflow forms a cycle between CG and FGR, hence, is named altogether as Cycle Coarse Graining (CCG), and provides a novel and self-consistent framework for multiscale molecular modelling.

### III. RESULTS

#### 1. Benchmark cycle coarse graining on numerical potentials

We first benchmarked CCG on a 2-dimensional numerical model and illustrated how it works with different settings. The potential energy surface  $U(x, y)$  of Tiwary-Berne model [44] is shown in Fig. 1a, which consists of three local minima. The optimal linear reaction coordinate  $s = x \cos \alpha + y \sin \alpha$  (where  $\alpha = 81.5^\circ$  is the skewing angle from  $x$ -axis) for this model was derived by Tiwary et al. [44] (dashed line in Fig. 1a), and computing potential of mean force (PMF, or free energy) along  $s$  entails time-consuming simulations via either Monte Carlo or Langevin dynamics. Although being simple, this model is characteristic of many bio-physical systems composed of multiple metastable states and the interstate transitions are rare events. We thus treated

$s$  as the CG variable and tried to reconstruct  $(x, y)$  given the 1-dimensional  $s$ .

We first performed energy-based training for FGR according to Eq. (5). We adopted FFJORD [45], one type of deep bijectors to model the generative distribution  $q_\theta(x, y; s)$ , and randomly sampled  $s$  according to a uniform distribution between  $[-0.5, 1.5]$ . Since  $s$  is linear function of  $(x, y)$ , we resorted to substitution-of-variables instead of consistency regularization, rigorously satisfying the constraint (see more details about training and model setup in SI). Given the optimized  $q_\theta$ , we computed the variational free energy along  $s$  according to Eq. (10). Figure 1b shows the resulting variational free energy profile learned by CCG, which has neither performed rare event sampling nor required transitions between metastable states. However, the accuracy is remarkably good compared to the reference PMF which is computed by integrating over the true potential energy surface, showing that CCG enables free energy calculation or coarse graining in a rare-event-free approach.

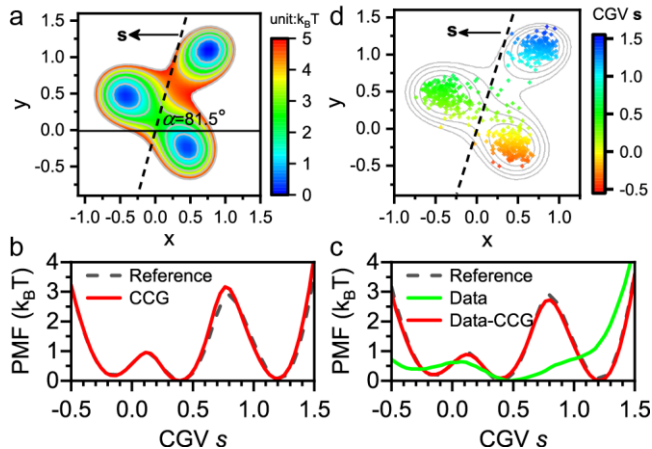


**FIG. 1** Illustration of cycle coarse graining (CCG) on a numerical model. (a) The potential energy surface (PES) of the model, shown in colored contour plot. The dashed line indicates the linear reaction coordinate  $s$  with a skewing angle  $\alpha$ . (b) The potential of mean force (PMF) computed by energy-trained CCG (red line) compared to ground-truth reference (black dashed line). (c) The potential of mean force computed by data-trained CCG (red line) compared to ground-truth reference (black dashed line). Distribution of the off-equilibrium data is also shown (green line). (d) Generated data through factorized sampling using energy-trained CCG model, colored according to the CG variable  $s$  during FGR. The PES is shown as grey contours in background.

We also benchmarked data-based FGR. To simulate better the real-world cases, we assumed that the accessible data of  $(x, y)$  are distributed off equilibrium. To do so, we ran Langevin dynamics simulation with much higher temperature and collected the samples as shown in Fig. S1b, and the corresponding data distribution along  $s$  is shown by green line in Fig. 1c which deviates dramatically from the reference as expected. Besides, we tested the strength of cycle loss ( $\lambda$  in Eq. (8)) ranging from  $10^{-4}$  to 1, and found

that training was robust with respect to the choice of  $\lambda$ . Particularly, even if the regularization strength was set to be rather weak ( $\lambda = 10^{-4}$ ), the consistency regularizer still converged much faster than the generative objective, and achieved negligible errors after training (Fig. S1a), indicating that a small  $\lambda$  would suffice for the relaxed FGR objective.

Given that the training data is off-equilibrium, we optimized FFJORD according to Eq. (S16), a modified version of Eq. (6) with reweighting trick, and applied correction to the variational free energy according to Zwanzig’s free-energy perturbation theory [46] (Eq. (S17); see SI for more details). Figure 1c shows that the resulting free energy profile along  $s$  agrees well with the reference, demonstrating that CCG can rescue free energy calculations even if the training data is distributed far off equilibrium.

To generate samples from  $U(x, y)$ , we can perform factorized sampling based on the CG potential  $F_\theta(s)$  according to Eq. (9). We first conducted Monte Carlo sampling of  $s$  according to  $F_\theta(s)$ , then performed FGR with

an optimized  $q_\theta(x, y; s)$ . The generated samples from an energy-trained  $q_\theta$  is shown in Fig. 1d, which conform to the correct Boltzmann distribution. Similar results were also obtained for models trained by data-based objective (Fig. S1c).

Finally, we can generate fake trajectories connecting metastable states by interpolating or extrapolating the CG variable  $s$ , and we term this technique as “*trajectory interpolation*”. Trajectory interpolation can be done simply by fixing the random variable  $\mathbf{z}$  of the generative model  $f_\theta(\mathbf{z}; \mathbf{s})$  (Eq. (7)) while varying the conditional variable  $\mathbf{s}$  as desired, then recording the corresponding output of the model  $\mathbf{R} = f_\theta(\mathbf{z}; \mathbf{s})$ . By selecting different random variables  $\mathbf{z}$  and performing trajectory interpolation for each  $\mathbf{z}$ , one can obtain an ensemble of fake trajectories. We showcased such a fake trajectory generated by interpolation in Fig. S1d, which connects all the three metastable states and passes through barriers between them, implying the possible application of this technique for investigating the transition states of chemical reactions.

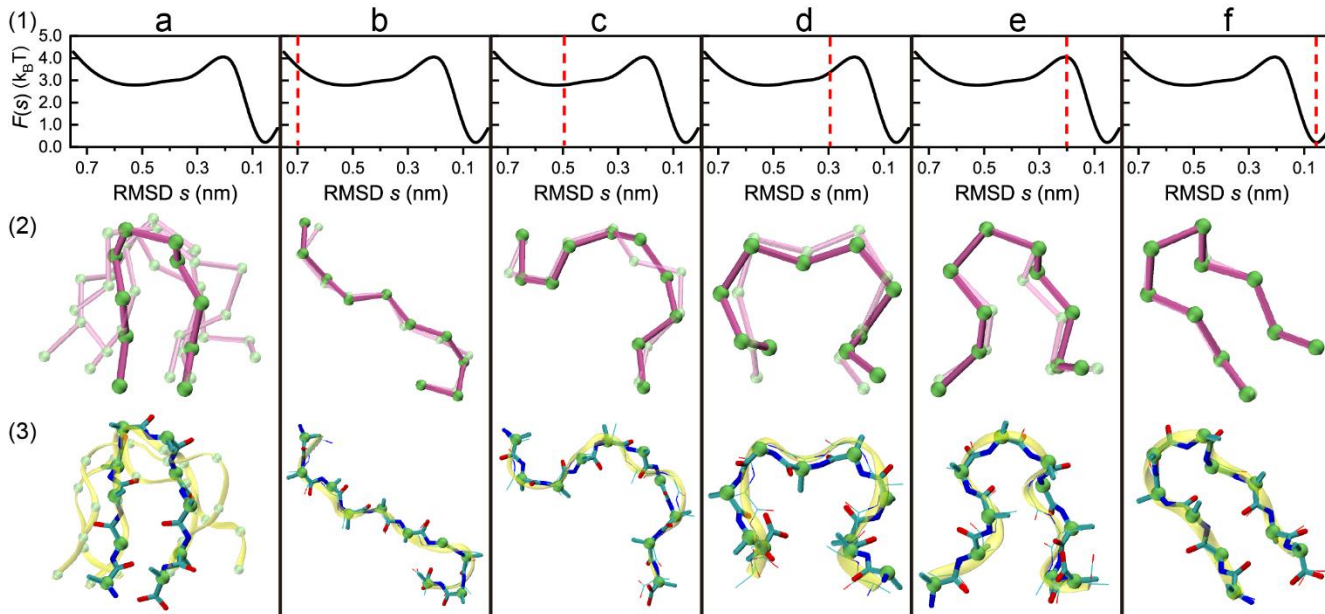


**FIG. 2** Multiscale fine-grained reconstruction for Chignolin. **Row 1:** (a) The PMF along the CG variable  $s$ , i.e., RMSD with respect to the native structure. (b) to (f) Five selected RMSD values at which the FGR results are inspected; (b), (c) and (d) correspond to unfolded states, (e) to the folding transition state and (f) is the folded state. **Row 2:** (a) Ca-structures are reconstructed given specified RMSD values. (b) to (f) show reconstructed  $C\alpha$  structures (opaque magenta) by trajectory interpolation at corresponding RMSD in Row 1; The best aligned MD structure is shown in transparency. **Row 3:** (a) Structures with backbone heavy atoms (BH-structures) are reconstructed from Ca-structures. (b) to (f) show BH-structures reconstructed from the corresponding Ca-structures in Row 2; The best aligned MD structure is shown as transparent yellow ribbons.

## 2. Cascaded fine-grained reconstruction for proteins

We then applied CCG for a mini-protein chignolin [47]. To verify the generic applicability of CCG, we performed FGR for chignolin at two different scales. At the first scale, the root-mean-squared deviation (RMSD) of  $C\alpha$  atoms from the native structure is treated as the 1-dimensional CG

variable  $\mathbf{s}$ , and all the  $C\alpha$  positions (denoted by  $\mathbf{r}$ ) are reconstructed, giving rise to  $C\alpha$  structures. Note that RMSD is a non-linear CG mapping, so reconstruction of  $C\alpha$  structures from RMSD values is not straightforward using existing methods. One commonly adopted approach is targeted MD which samples possible protein structures

under restraints of RMSD. However, targeted MD is very time-consuming, and depends severely on initial conditions and other hyperparameters like restraint strength; worse still, it can neither guarantee the diversity of reconstructed structures, nor the consistency with respect to the RMSD values. In contrast, we will show that CCG can efficiently reconstruct diverse FG samples of high quality and consistency.

We performed data-based training of a generative  $\mathbf{r} = f_{\theta_1}(\mathbf{z}; \mathbf{s})$  (Eq. (7)) using all-atom trajectories contributed by Lindorff-Larsen et al. [48] and applied consistency regularization (see more training details in SI). After training is done, we can generate  $C\alpha$  protein structures at a certain RMSD by feeding a random variable  $\mathbf{z}$  (drawn from standard normal distribution) and the specified  $\mathbf{s} = \text{RMSD}$  to  $f_{\theta_1}(\mathbf{z}; \mathbf{s})$ . Figure 2 Row 1 shows the equilibrium free energy profile along  $\mathbf{s}$  computed from the long MD simulations (Column a). Various reconstructed structures can be reconstructed at any specific  $\mathbf{s}$  by means of CCG as shown in Row 2 in Figure 2. Particularly, we selected five milestones along the RMSD profile (Column b to f in Fig. 2 Row 1) at which the reconstructed structures were inspected. Three of the five states (Column b to e) correspond to unfolded states which exhibit large RMSD with respect to the native structure, one state (Column f) corresponds to folded structure, and one (Column e) resides nearby the “transition state” of folding. Figure 2 Row 2 shows a fake trajectory interpolated along the five selected milestones: When RMSD is relatively large, extended conformations are generated; the hairpin-like structure forms near the transition state and a folded structure is yielded when RMSD approaches zero. We also verified that the generated structures given by CCG can be aligned reasonably with a counterpart found in real MD simulations, further validating the quality of these reconstructed structures.

Next, we performed CCG at another scale, where backbone structures (denoted by  $\mathbf{R}$ ) are reconstructed from a given  $C\alpha$  structure  $\mathbf{r}$ , with all backbone heavy atoms being added. Since this is a linear FGR problem, we trained the generative model  $\mathbf{R} = f_{\theta_2}(\mathbf{z}; \mathbf{r})$  according to the data-based objective without applying consistency regularization.

Now these two FGR models can be cascaded and generate FG structures at multiple scales given a certain RMSD: We first specified a RMSD value and generated  $C\alpha$  structures  $\mathbf{r}$  with  $f_{\theta_1}(\mathbf{z}; \mathbf{s})$ , then generated backbone structures  $\mathbf{R}$  with  $f_{\theta_2}(\mathbf{z}; \mathbf{r})$ . Put together, backbone structures can be generated according to a certain RMSD. Following this way, backbone structures are generated corresponding to the selected  $\mathbf{s}$  and  $\mathbf{r}$ , which are shown in Fig. 2 Row 3. In Figure S2, we presented more reconstructed structures generated through cascaded trajectory interpolation. It can be found that when RMSD approaches zero, the generated structures aligned better with each other, showing convergence of conformations in the folded state. Conversely, when RMSD

is large, the entropic effect dominates, and an increment of conformational diversity and flexibility is observed.

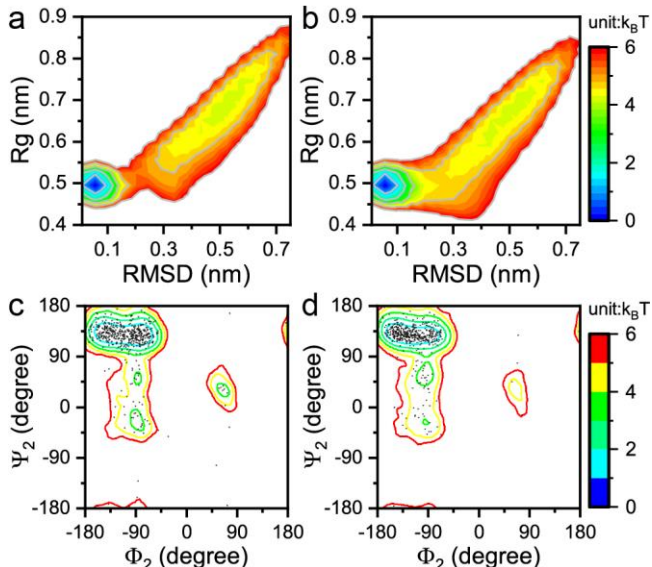


**FIG. 3** Conformational distribution of Chignolin through factorized sampling. The 2D free-energy plot for RMSD (with respect to native structure) and radius of gyration is drawn for MD samples (a) and factorized sampling (b), respectively. The Ramachandra plot for the 2<sup>nd</sup> residue is drawn for MD samples (c) and factorized sampling (d), respectively.

It is also appealing to examine whether multiscale factorized sampling of protein backbone structures satisfy the thermodynamic consistency principle in Eq. (4). Because conformations of proteins are of particular research interest, we compared the distribution of RMSD and radius of gyration (both are global characterizations of protein conformations) of generated structures against samples from equilibrium all-atom MD simulations, as shown in Fig. 3a and 3b. Furthermore, we are often concerned with the detailed local structures of a protein, so we showed the Ramachandra plots of all the torsional angles for backbone structures generated by factorized sampling and compared them with samples from long MD simulations (Fig. 3d and 3e, Fig. S3). As Figure 3 shows, the conformations generated via factorized sampling reproduce those sampled via long MD simulations, proving the thermodynamic consistency of CCG. This implies that by virtue of CCG, knowing the PMF along a low-dimensional CG variable or collective variable like RMSD may suffice for obtaining more detailed conformational statistics of a protein.

### 3. Rare-event-free sampling for chemical reactions

Since trajectory interpolation circumvents sampling of rare events, it can be particularly useful in the studies of many biophysical processes involving rare transition events. As an important case, simulation of chemical reactions is often hindered by two major challenges: 1) chemical

transitions are rare events due to high reaction barriers, thus a redundant number of single-point energy calculations are needed; 2) evaluation of the single-point energy involves quantum calculations which are slow and expensive. Recent advent of machine-learned potential [49,50] could help soothe the latter issue, by providing a surrogate potential to the quantum oracle which can be evaluated much faster. However, optimization of the surrogate potential requires training labels covering all the relevant reaction phase space with reference to the oracle [51], which entails exploration over the reaction coordinates and sampling of rare events. We will show that CCG can be employed to solve these issues effectively following an active learning workflow (Fig. 4) and the training protocol is summarized in SI and Algorithm S2.

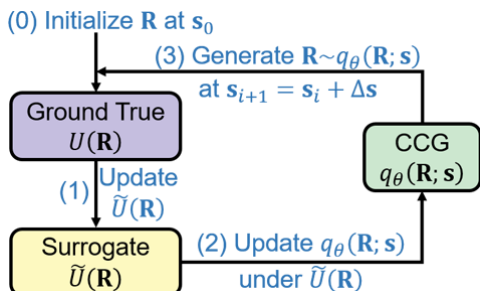


**FIG. 4** Rare-event-free workflow for active learning of chemical reactions via CCG. In one iteration, the all-atom structures  $\mathbf{R}$ , generated by either initialization or CCG, are fed to oracle quantum potential function and yield training labels  $U(\mathbf{R})$ . The surrogate machine-learned potential  $\tilde{U}(\mathbf{R})$  is updated by supervision of these labels. The CCG model  $q_\theta(\mathbf{R}; \mathbf{s})$  is then updated based on  $\tilde{U}(\mathbf{R})$ , and generates new samples by extrapolating the reaction coordinates  $\mathbf{s}$ , which are labeled during next iteration.

As Fig. 4 illustrates, given initial configurations  $\mathbf{R}$ , we first label them by calling the oracle  $U(\mathbf{R})$ , then train the surrogate function  $\tilde{U}(\mathbf{R})$  using these labels and update the CCG model  $q_\theta(\mathbf{R}; \mathbf{s})$  with respect to  $\tilde{U}(\mathbf{R})$ . This allows us to quickly obtain diverse samples along  $\mathbf{s}$  without performing rare-event sampling. These samples are further queried by the oracle and form new labels for the surrogate potential. Hence, the CCG model  $q_\theta$  and the surrogate potential  $\tilde{U}$  can be optimized in an alternating manner. When both models converge, the free energy profile along  $\mathbf{s}$  as well as molecular configurations can be directly obtained from  $q_\theta$  without performing MD simulations.

To examine whether CCG can help study chemical reactions in a computationally cheap and rare-event-free manner, we applied this strategy (Fig. 4) to investigate a textbook reaction, the substitution between  $\text{Cl}^-$  and  $\text{CH}_3\text{Cl}$  (Fig. 5a) which is known to undergo a typical  $\text{S}_{\text{N}}2$  mechanism. The positions of three reactive atoms ( $\text{Cl}^-$ ,  $\text{Cl}$  and  $\text{C}$ ) are selected as the CG variable  $\mathbf{s}$ , and we transformed the Cartesian coordinates into three internal coordinates (Fig. 5a), namely, the lengths of two C-Cl bonds ( $d_1, d_2$ ) and the C-Cl-C reaction angle ( $\alpha$ ), which suffice to describe the

relative positions of these three atoms. We trained the surrogate potential as a function of all atom positions to approximate the reference atomic forces and energies, and employed a deep bijective model as  $q_\theta(\mathbf{R}; \mathbf{s})$  which output all atom positions  $\mathbf{R}$  including hydrogens (see SI for more details).

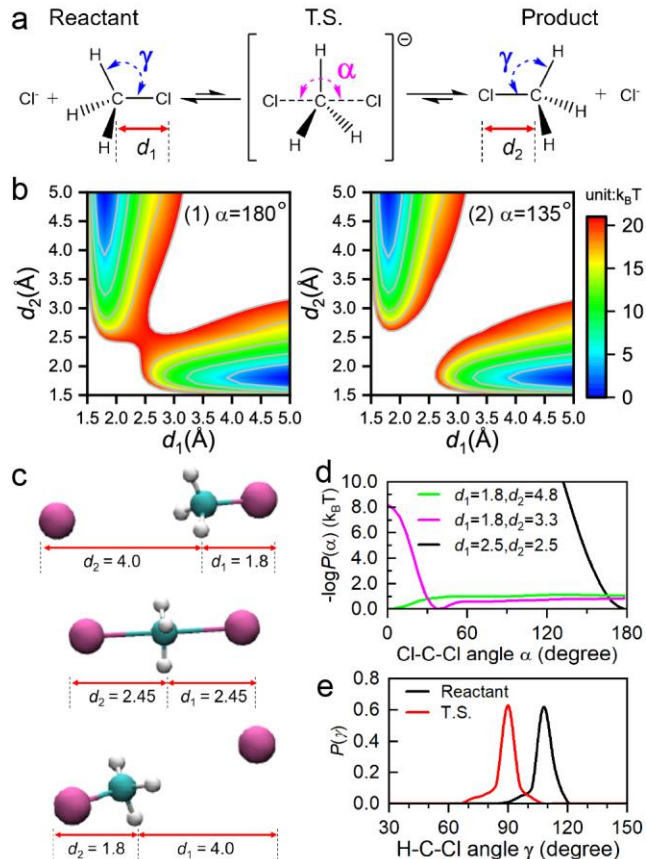


**FIG. 5** Rare-event-free sampling of  $\text{S}_{\text{N}}2$  reaction: the substitution between  $\text{Cl}^-$  and  $\text{CH}_3\text{Cl}$ . (a) Scheme of the reaction, where reactant, product and transition state complex (T.S.) is shown. Important structural descriptors are also illustrated, including the lengths of two C-Cl bonds ( $d_1$  and  $d_2$ , respectively), Cl-C-Cl angle ( $\alpha$ ) and H-C-Cl angle ( $\gamma$ ). (b) Free-energy surface spanned by the two C-Cl bond lengths at different Cl-C-Cl reaction angles:  $\alpha = 180^\circ$  (left),  $\alpha = 135^\circ$  (right). (c) Snapshots of atomic structures through trajectory interpolation, including reactant (top), transition state (middle) and product (bottom); Carbons are colored by cyan, chlorides by magenta, and hydrogens by white. (d) Distribution of Cl-C-Cl reaction angle  $\alpha$  at different reaction stages. (e) Distribution of H-C-Cl angle  $\gamma$  in reactant (black) and transition state (red).

After training, we can draw samples at given  $\mathbf{s}$  and compute the variational free energy according to Eq. (10). The free energy surface (FES) is plotted at different reaction angles ( $\alpha$ ) in Fig. 5b. Because this reaction is symmetric with respect to two Cl atoms, the FES appears symmetric as expected. At  $\alpha = 180^\circ$  where C-Cl-C reside on a straight line, there is a unique saddle point across the FES residing at

about  $d_1 = d_2 \approx 2.45 \text{ \AA}$ , indicating that bond breaking is synchronized with bond forming, consistent with a  $S_N2$  mechanism. However, when we changed  $\alpha$  to  $135^\circ$ , mimicking the reaction triggered by non-straight collisions (Fig. 5b), although the FES at product or reactant region does not change significantly, the saddle point region, which is key to the reactivity, is dramatically leveled up, excluding the possibility of such reaction pathways.

Next, we interpolated linearly between  $d_1$  and  $d_2$  with  $\alpha$  fixed at  $180^\circ$ , and Fig. 5c shows the all-atom structures, which are generated by the optimized  $q_\theta$ , of the reactant, product, and transition state along an interpolated trajectory. Noteworthy, these structures exhibit authentic chemical details. For instance, the  $\text{CH}_3\text{Cl}$  molecules in reactant or product both show a tetrahedron shape in agreement with a  $\text{sp}^3$  central carbon. However, for the transition state (TS) complex, the hydrogens become planar with respect to the central carbon, and they form trigonal bipyramid together with the two Cl atoms. To verify whether the chemical details are generally preserved as reaction proceeds, we performed factorized sampling and generated all-atom structures at different  $\mathbf{s}$ . The distribution of the angle  $\alpha$  was computed based on these samples (Fig. 5d). It can be seen that, when Cl<sup>-</sup> is far away from  $\text{CH}_3\text{Cl}$  (i.e.,  $d_2 > 4 \text{ \AA}$ ), its orientation with respect to the other C-Cl bond is relatively arbitrary and isotropic. When Cl<sup>-</sup> approaches the reactive center (characterized by a shortened  $d_2$  value), its orientation with respect to C-Cl bond becomes more restrained. When the TS complex is formed, the C-Cl-C angle becomes highly restrained and only  $\alpha \approx 180^\circ$  is allowed (i.e., three atoms in a line). Similarly, we also showed the distribution of H-C-Cl angle ( $\gamma$ ) in Fig. 5e. In reactant or product, angle  $\gamma$  stays around  $110^\circ$ , corresponding to a  $\text{sp}^3$ -hybridized carbon. But in the TS complex (defined as  $d_1, d_2 \leq 2.55 \text{ \AA}$ ), this angle shifts to about  $90^\circ$ , indicating that Cl-C bond is orthogonal to the  $\text{CH}_3$  planar, which also agree well with the chemical fact.

#### IV. CONCLUDING REMARKS

Multiscale molecular modeling is very useful in molecular science where molecular properties at large time and lengths scales are of interest. But its application is limited by two long-standing challenges: One is to construct coarse-grained models by proper abstraction of fine-scaled models; the other is to restore finer molecular details given coarse-grained configurations. Although these two problems are commonly addressed independently, in this work, we presented a theory connecting them, and developed CCG to solve both problems in a consistent manner.

In CCG, we formulated fine-grained reconstruction as a probabilistic learning problem, and delivered a tractable solution to this task by means of machine learning. Through experiments we demonstrated that CCG is a reliable strategy for high throughput and high accuracy conversion of CG

structures into FG ones for complex biophysical processes like protein folding and chemical reactions. Moreover, CCG provides a rare-event-free approach to coarse graining or free energy calculations. Specifically, trajectory interpolation enables fast exploration of the CG space that governs the slow motions of the system, whereas conventional MD simulations would be inefficient in sampling these transitions involving rare events. On the other hand, by separating the slow coarse-grained or collected motions and fast fine-grained DoFs, factorized sampling leads to a rigorous multiscale approach to expediting the investigation of equilibrium properties of complex systems.

The methodology presented in this paper can be easily extended to other biophysical systems at different coarse-graining levels, such as biomacromolecules and polymers, where tuning atomistic details via human intervention is particularly labor-intensive. Besides, trajectory interpolation as well as factorized sampling makes it easy to marry other pathway-searching techniques like milestone [52] and string method [42]. Although the generative models employed in this paper are all bijective, various quasi-invertible models [53,54] have been developed by the machine learning community recently, and they can help extending the application scope of CCG. In addition to thermodynamic consistency discussed throughout this paper, CG or FGR pursuing correct dynamics is also an active research field. Some recent efforts proposed machine learning approaches to extract dynamic information from molecular simulation trajectories [55,56], where CCG may also deliver helpful solutions, and we leave this direction to further studies.

#### ACKNOWLEDGEMENTS

This research was supported by Science & Technology Innovation 2030 - New Generation of Artificial Intelligence 2022 Major Program (No. 2022ZD0115003), National Natural Science Foundation of China (22050003, 92053202, 21821004, 21927901 to Y.Q.G.). The authors thank Dr. Yi Isaac Yang and Yifan Li for useful discussion. J.Z. also thanks the Tiger supercomputer cluster in Princeton University.

#### REFERENCES

- 
- [1] D. Frenkel and B. Smit, *Understanding molecular simulation: from algorithms to applications* (Elsevier, 2001), Vol. 1.
  - [2] L. Monticelli, S. K. Kandasamy, X. Periole, R. G. Larson, D. P. Tieleman, and S.-J. Marrink, *Journal of chemical theory and computation* **4**, 819 (2008).
  - [3] M. G. Saunders and G. A. Voth, *Annual review of biophysics* **42**, 73 (2013).

- [4] G. Fiorin, M. L. Klein, and J. Héning, *Molecular Physics* **111**, 3345 (2013).
- [5] W. Noid, J.-W. Chu, G. S. Ayton, V. Krishna, S. Izvekov, G. A. Voth, A. Das, and H. C. Andersen, *The Journal of chemical physics* **128**, 244114 (2008).
- [6] G. M. Torrie and J. P. Valleau, *Journal of Computational Physics* **23**, 187 (1977).
- [7] C. Abrams and G. Bussi, *Entropy* **16**, 163 (2014).
- [8] Y. Okamoto, *Journal of Molecular Graphics and Modelling* **22**, 425 (2004).
- [9] Y. I. Yang, Q. Shao, J. Zhang, L. Yang, and Y. Q. Gao, *The Journal of Chemical Physics* **151**, 070902 (2019).
- [10] D. Reith, M. Pütz, and F. Müller - Plathe, *Journal of computational chemistry* **24**, 1624 (2003).
- [11] S. Izvekov and G. A. Voth, *The Journal of Physical Chemistry B* **109**, 2469 (2005).
- [12] M. S. Shell, *The Journal of chemical physics* **129**, 144108 (2008).
- [13] E. Schneider, L. Dai, R. Q. Topper, C. Drechsel-Grau, and M. E. Tuckerman, *Physical review letters* **119**, 150601 (2017).
- [14] J. Wang, S. Olsson, C. Wehmeyer, A. Pérez, N. E. Charron, G. De Fabritiis, F. Noé, and C. Clementi, *ACS central science* (2019).
- [15] J. Zhang, Y.-K. Lei, Y. I. Yang, and Y. Q. Gao, *The Journal of Chemical Physics* **153**, 174115 (2020).
- [16] J. Köhler, Y. Chen, A. Krämer, C. Clementi, and F. Noé, arXiv preprint arXiv:2203.11167 (2022).
- [17] Y. I. Yang and Y. Q. Gao, *The Journal of Physical Chemistry B* **119**, 662 (2015).
- [18] K. Johnston and V. Harmandaris, *Soft Matter* **9**, 6696 (2013).
- [19] E. Weinan and B. Engquist, *Communications in Mathematical Sciences* **1**, 87 (2003).
- [20] A. P. Heath, L. E. Kavrakı, and C. Clementi, *Proteins: Structure, Function, and Bioinformatics* **68**, 646 (2007).
- [21] T. A. Wassenaar, K. Pluhackova, R. A. Böckmann, S. J. Marrink, and D. P. Tieleman, *Journal of chemical theory and computation* **10**, 676 (2014).
- [22] L. E. Lombardi, M. A. Martí, and L. Capece, *Bioinformatics* **32**, 1235 (2016).
- [23] L.-J. Chen, H.-J. Qian, Z.-Y. Lu, Z.-S. Li, and C.-C. Sun, *The Journal of Physical Chemistry B* **110**, 24093 (2006).
- [24] J. Schlitter, M. Engels, and P. Krüger, *Journal of molecular graphics* **12**, 84 (1994).
- [25] W. Yang, X. Zhang, Y. Tian, W. Wang, J.-H. Xue, and Q. Liao, *IEEE Transactions on Multimedia* **21**, 3106 (2019).
- [26] W. Li, C. Burkhardt, P. Políńska, V. Harmandaris, and M. Doxastakis, *The Journal of Chemical Physics* **153**, 041101 (2020).
- [27] F. Noé, S. Olsson, J. Köhler, and H. Wu, *science* **365** (2019).
- [28] I. Goodfellow, J. Pouget-Abadie, M. Mirza, B. Xu, D. Warde-Farley, S. Ozair, A. Courville, and Y. Bengio, in *Advances in neural information processing systems* (2014), pp. 2672.
- [29] D. P. Kingma and M. Welling, arXiv preprint arXiv:1312.6114 (2013).
- [30] D. M. Blei, A. Kucukelbir, and J. D. McAuliffe, *Journal of the American Statistical Association* **112**, 859 (2017).
- [31] D. J. Rezende and S. Mohamed, arXiv preprint arXiv:1505.05770 (2015).
- [32] J. Sohl-Dickstein, E. Weiss, N. Maheswaranathan, and S. Ganguli, in *International Conference on Machine Learning* (PMLR, 2015), pp. 2256.
- [33] R. D. Hills Jr, L. Lu, and G. A. Voth, *PLoS computational biology* **6**, e1000827 (2010).
- [34] A. Abdolmaleki, J. T. Springenberg, J. Degraeve, S. Bohez, Y. Tassa, D. Belov, N. Heess, and M. Riedmiller, arXiv preprint arXiv:1812.02256 (2018).
- [35] C. Lemaréchal, in *Computational combinatorial optimization* (Springer, 2001), pp. 112.
- [36] J.-Y. Zhu, T. Park, P. Isola, and A. A. Efros, in *Proceedings of the IEEE international conference on computer vision* (2017), pp. 2223.
- [37] X. Chen, Y. Duan, R. Houthoof, J. Schulman, I. Sutskever, and P. Abbeel, *Advances in neural information processing systems* **29** (2016).
- [38] Y. Sugita and Y. Okamoto, *Chemical physics letters* **314**, 141 (1999).
- [39] Y. Q. Gao, *The Journal of chemical physics* **128**, 064105 (2008).
- [40] A. Laio and M. Parrinello, *Proceedings of the National Academy of Sciences* **99**, 12562 (2002).
- [41] L. Zhang, H. Wang, and W. E, *The Journal of chemical physics* **148**, 124113 (2018).
- [42] E. Weinan, W. Ren, and E. Vanden-Eijnden, *J. Phys. Chem. B* **109**, 6688 (2005).
- [43] J. Zhang, Y.-K. Lei, Z. Zhang, X. Han, M. Li, L. Yang, Y. I. Yang, and Y. Q. Gao, *Physical Chemistry Chemical Physics* **23**, 6888 (2021).
- [44] P. Tiwary and B. Berne, *The Journal of chemical physics* **147**, 152701 (2017).
- [45] W. Grathwohl, R. T. Q. Chen, J. Bettencourt, I. Sutskever, and D. Duvenaud, in *International Conference on Learning Representations* (2019).
- [46] R. Zwanzig, *Nonequilibrium statistical mechanics* (Oxford University Press, 2001).
- [47] S. Honda, K. Yamasaki, Y. Sawada, and H. Morii, *Structure* **12**, 1507 (2004).
- [48] K. Lindorff-Larsen, S. Piana, R. O. Dror, and D. E. Shaw, *Science* **334**, 517 (2011).
- [49] J. Behler, *journal of chemical physics* **145** (2016).
- [50] A. P. Bartók, S. De, C. Poelking, N. Bernstein, J. R. Kermode, G. Csányi, and M. Ceriotti, *Science advances* **3**, e1701816 (2017).

- [51] L. Zhang, J. Han, H. Wang, R. Car, and E. Weinan, *Physical review letters* **120**, 143001 (2018).
- [52] A. K. Faradjian and R. Elber, *The Journal of chemical physics* **120**, 10880 (2004).
- [53] Y. Song, J. Sohl-Dickstein, D. P. Kingma, A. Kumar, S. Ermon, and B. Poole, arXiv preprint arXiv:2011.13456 (2020).
- [54] Y. Lipman, R. T. Chen, H. Ben-Hamu, M. Nickel, and M. Le, arXiv preprint arXiv:2210.02747 (2022).
- [55] H. Wu, A. Mardt, L. Pasquali, and F. Noe, in *Advances in Neural Information Processing Systems*2018), pp. 3975.
- [56] H. Sidky, W. Chen, and A. L. Ferguson, *Chemical Science* **11**, 9459 (2020).
- [57] L. Dinh, D. Krueger, and Y. Bengio, arXiv preprint arXiv:1410.8516 (2014).
- [58] L. Dinh, J. Sohl-Dickstein, and S. Bengio, in *International Conference on Learning Representations*2017).
- [59] M. Germain, K. Gregor, I. Murray, and H. Larochelle, in *International Conference on Machine Learning*2015), pp. 881.
- [60] G. Papamakarios, T. Pavlakou, and I. Murray, in *Neural Information Processing Systems*2017), pp. 2338.
- [61] Y. P. Huang, Y. Xia, L. Yang, J. Wei, Y. I. Yang, and Y. Q. Gao, *Chinese Journal of Chemistry* **40**, 160 (2022).
- [62] S. S. Schoenholz and E. D. Cubuk, *bulletin of the american physical society* (2019).

## Supplemental Information

### Machine-Learned Invertible Coarse Graining for Multiscale Molecular Modeling

Jun Zhang<sup>1,†</sup>, Xiaohan Lin<sup>2</sup>, Weinan E<sup>3,4</sup> and Yi Qin Gao<sup>1,2</sup>

<sup>1</sup> *Changping Laboratory, Beijing 102200, China*

<sup>2</sup> *Beijing National Laboratory for Molecular Sciences, College of Chemistry and Molecular Engineering, Peking University, Beijing 100871, China*

<sup>3</sup> *AI for Science Institute, Beijing, China*

<sup>4</sup> *Center for Machine Learning Research and School of Mathematical Sciences, Peking University, Beijing 100871, China*

Correspondence should be sent to: † jzhang@cpl.ac.cn (Jun Zhang)

## PART I. SUPPLEMENTAL TEXTS

### I. Training objectives of cycle coarse graining (CCG)

#### A. Kullback-Leibler divergence

$$D_{\text{KL}}(p \parallel p_\theta) = \int p(\mathbf{s}) \log \left( \frac{p(\mathbf{s})}{p_\theta(\mathbf{s})} \right) d\mathbf{s} \quad (\text{S1})$$

where both distributions are assumed to admit densities (i.e. absolutely continuous) with respect to a same measure. KL divergence is known to be strict, which means that

$$D_{\text{KL}}(p \parallel p_\theta) \geq 0$$

$$D_{\text{KL}} = 0 \text{ if and only if } p = p_\theta$$

Besides, KL divergence is known to be asymmetric, i.e.  $D_{\text{KL}}(p \parallel p_\theta) \neq D_{\text{KL}}(p_\theta \parallel p)$ , and possibly infinite when there is non-overlapping area between the two distributions.

#### B. Deep bijective models

Given a random variable  $\mathbf{z} \sim q(\mathbf{z})$  and a function  $f_\psi: \mathbb{R}^D \rightarrow \mathbb{R}^D$  that bijectively maps  $\mathbf{z}$  into  $\mathbf{s}$ , where  $D = \text{Dim}(\mathbf{s}) = \text{Dim}(\mathbf{z})$ , then the probability of the random variable  $\mathbf{s}$  can be computed according to the change-of-variables formula:

$$\begin{aligned} \mathbf{s} &= f_\theta(\mathbf{z}) \\ \mathbf{z} &= f_\theta^{-1}(\mathbf{s}) \end{aligned} \quad (\text{S2})$$

$$\log q_\theta(\mathbf{s}) = \log q(\mathbf{z}) - \log \left| \det \left( \frac{\partial f_\theta}{\partial \mathbf{z}} \right) \right|$$

Calculating  $q_\psi(\mathbf{s})$  using Eq. (S2) admits two key premises: (i)  $q(\mathbf{z})$  is tractable so that drawing samples of  $\mathbf{z}$  can be achieved with ease; (ii) the bijective function  $f_\psi$  has a tractable Jacobian whose determinant can be computed efficiently. In practice, one can simply choose a normal distribution as  $q(\mathbf{z})$  to meet the first requirement. However, the computational cost of the determinant of the Jacobian of a bijective function generally scales as  $\mathcal{O}(D^3)$ , so ANNs of special architectures are needed for the second requirement.

Deep generative models that satisfy these two requirements include but not limited to normalizing-flow models [31,57,58] auto-regressive flow models [59,60], and we refer readers interested in this topic to the references.

#### C. Training objectives

We first review the energy-based objective (Eq. (5) in the main text), where  $p$  denotes the target reconstruction distribution and  $q_\theta$  denotes the optimizable generative distribution,

$$\nabla_\theta D_{\text{KL}}(q_\theta \parallel p) = \mathbb{E}_{\mathbf{R} \sim q_\theta} [\nabla_\theta \log q_\theta(\mathbf{R}; \mathbf{s}) + \beta \nabla_\theta U(\mathbf{R}; \mathbf{s})] \quad (\text{S3})$$

It should be noted that implementing Eq. (S3) requires the energy term  $U(\mathbf{R})$  be differentiable with respect to model parameters. That is, the energy and force functions should be built in the computational graph of an auto-differentiation framework like Tensorflow or Pytorch. Therefore, an auto-differentiable MD simulation package like MindSPONGE [61] or JAX-MD [62] is needed in order to support energy-based training.

On the other hand, data-based training can be performed without calling force-computing functions, instead, it assumes sufficient paired samples of CG and FG structures are accessible,

$$\nabla_\theta D_{\text{KL}}(p \parallel q_\theta) \approx \mathbb{E}_{\mathbf{R} \in \mathcal{D}} [-\nabla_\theta \log q_\theta(\mathbf{R}; \mathbf{s})] \quad (\text{S4})$$

In some cases when the energy or force function is callable and paired samples are also provided, we can adopt a mix objective by linearly combining Eq. (S3) and Eq. (S4),

$$\nabla_\theta \mathcal{L}(\theta) = (1 - \eta_1) \nabla_\theta D_{\text{KL}}(q_\theta \parallel p) + \eta_1 \nabla_\theta D_{\text{KL}}(p \parallel q_\theta) \quad (\text{S5})$$

where  $\eta_1 \in [0, 1]$  balances the two loss terms.

Besides, since we have the analytical form of the variational free energy along CG variable  $\mathbf{s}$  (Eq. (10) in the main text), the expression for the mean force along  $\mathbf{s}$  ( $-\nabla_{\mathbf{s}} F_\theta(\mathbf{s})$ ) can be derived as follows,

$$\nabla_{\mathbf{s}} F_\theta(\mathbf{s}) = \mathbb{E}_{\mathbf{z}} \nabla_{\mathbf{s}} [\beta^{-1} \log q_\theta(f_\theta(\mathbf{z}; \mathbf{s})) + U(f_\theta(\mathbf{z}; \mathbf{s}))] \quad (\text{S6})$$

which can be computed straightforwardly using any auto-differentiation techniques. Equipped with Eq. (S6), we can further augment the training objective with force matching, which is widely adopted in supervised-learning CG approaches [13,14,41], provided that labels of mean forces,  $\nabla_{\mathbf{s}} F(\mathbf{s})$ , are accessible,

$$\mathcal{L}_{\text{aug}}(\theta) = \mathcal{L}(\theta) + \eta_2 \left\| \nabla_{\mathbf{s}} F_\theta(\mathbf{s}) - \nabla_{\mathbf{s}} F(\mathbf{s}) \right\|^2 \quad (\text{S7})$$

where  $\mathcal{L}(\theta)$  takes the same form as Eq. (S5) and  $\eta_2$  controls how much of the overall learning signal comes from the force-matching term.

Finally, we remark that the expectation involved in Eq. (S3) and Eq. (S4) are computed over both  $\mathbf{s}$  and  $\mathbf{R}$ , i.e.,

$$\mathbb{E}_{\mathbf{R} \sim q_\theta} [g(\mathbf{R})] := \mathbb{E}_{\mathbf{s} \sim q(\mathbf{s})} \mathbb{E}_{\mathbf{R} \sim q_\theta(\mathbf{z}; \mathbf{s})} [g(\mathbf{R})] \quad (\text{S8})$$

$$\mathbb{E}_{\mathbf{R} \sim \mathcal{D}} [g(\mathbf{R})] := \mathbb{E}_{\mathbf{s} \sim q(\mathbf{s})} \mathbb{E}_{\mathbf{R} \in \{\mathbf{R} \in \mathcal{D}; \mathbf{s}(\mathbf{R}) = \mathbf{s}\}} [g(\mathbf{R})]$$

where  $g(\cdot)$  is an arbitrary function of  $\mathbf{R}$ , and  $q(\mathbf{s})$  is a user-defined prior distribution over  $\mathbf{s}$ . Noteworthy, we do not

assume  $q(\mathbf{s})$  to be identical to  $p(\mathbf{s})$  (Eq. (1) in the main text). Instead, we can use any distribution which can be easily sampled from and covers well the CG space, for example, a uniform distribution, as  $q(\mathbf{s})$ .

## II. Variational free energy (VFE)

### A. Derivation of VFE

VFE can be developed through various approaches [30]. Here we briefly derive VFE according to Zwanzig's free energy perturbation (FEP) theory [46]. Given the reference potential energy function  $U(x)$  and a surrogate potential energy function  $U_\theta(x)$ , we can define the absolute reference free energy  $F$  and the approximate free energy  $\tilde{F}_\theta$  by Eq. (S9),

$$Z = \int e^{-\beta U(x)} dx; Z_\theta = \int e^{-\beta U_\theta(x)} dx$$

$$\beta F := -\log Z; \beta \tilde{F}_\theta := -\log Z_\theta \quad (\text{S9})$$

$$p(x) = e^{-\beta U(x)} / Z; q_\theta(x) = e^{-\beta U_\theta(x)} / Z_\theta$$

and we can compute the difference of  $\tilde{F}_\theta$  with respect to  $F$  by means of FEP,

$$\begin{aligned} \beta(\tilde{F}_\theta - F) &= \log \frac{Z}{Z_\theta} \\ &= \log \mathbb{E}_{x \sim q_\theta} \exp(-\beta(U(x) - U_\theta(x))) \\ &\geq \mathbb{E}_{x \sim q_\theta} [\log(\exp(-\beta(U(x) - U_\theta(x))))] \quad (\text{S10}) \\ &\quad (\text{Jensen's inequality}) \\ &= \mathbb{E}_{x \sim q_\theta} [\beta(U_\theta(x) - U(x))] \end{aligned}$$

Now consider the following definition translated from Eq. (S9),

$$\beta U_\theta(x) \equiv -\log q_\theta(x) - \log Z_\theta \quad (\text{S11})$$

and replace the corresponding terms in Eq. (S10) by Eq. (S11), we arrive at the conclusion,

$$\begin{aligned} \log Z - \log Z_\theta &\geq \mathbb{E}_{x \sim q_\theta} [-\log q_\theta(x) - \log Z_\theta - \beta U(x)] \\ \Rightarrow \log Z &\geq -\mathbb{E}_{x \sim q_\theta} [\log q_\theta(x) + \beta U(x)] \quad (\text{S12}) \\ \Rightarrow \log Z &= -\beta F \geq -\beta \tilde{F}_\theta \Rightarrow F_\theta \geq F \end{aligned}$$

$$\text{where } \beta \tilde{F}_\theta := \mathbb{E}_{x \sim q_\theta} [\log q_\theta(x) + \beta U(x)]$$

$F_\theta$  is known as the variational free energy, which forms an upper bound to the ground-truth free energy  $F$ .

### B. Neural importance sampling (NIS)

Given a bijective normalizing-flow model  $q_\theta(x)$  (by definition, the partition function of a normalizing-flow

model is unity), the surrogate energy function can be defined as,

$$\begin{aligned} \beta U_\theta(x) &:= -\log q_\theta(x) - \log Z_\theta \\ &= -\log q_\theta(x) \quad (\text{S13}) \\ &\quad (\text{note that } \log Z_\theta = 0) \end{aligned}$$

where  $\log q_\theta(x)$  can be easily computed via change-of-variable formula, i.e., Eq. (S2).

Therefore, to compute any expectation over  $p(x)$ , the Boltzmann distribution of the reference energy function  $U(x)$ , we can adopt the importance sampling technique,

$$\mathbb{E}_p[g(x)] = \mathbb{E}_{q_\theta} \left[ \frac{p(x)}{q_\theta(x)} g(x) \right] \quad (\text{S14})$$

where  $g(\cdot)$  is an arbitrary function of  $x$ , and the importance weight is given by,

$$\begin{aligned} \frac{p(x)}{q_\theta(x)} &\propto \exp[\beta U_\theta(x) - \beta U(x)] \\ &= \exp[-\log q_\theta(x) - \beta U(x)] \quad (\text{S15}) \end{aligned}$$

Note that implementation of Eq. (S14) requires merely samples from  $q_\theta(x)$  rather than  $p(x)$ . While sampling from  $p(x)$  is known to be difficult and often time-consuming, sampling from  $q_\theta(x)$  is straightforward thus computing expectation values in the right-hand side of Eq. (S14) is simple [27].

### C. Reweighted likelihood

To implement VFE in Eq. (10) or Eq. (S12) with a data-trained model  $q_\theta(\mathbf{R}; \mathbf{s})$ , we do not require global equilibrium over the CG variable  $\mathbf{s}$ . However, local equilibrium at any given  $\mathbf{s}$  is assumed. This requirement can be simply achieved by, for instance, umbrella sampling at  $\mathbf{s}$  [6]. If this requirement is not satisfied and the data is off-equilibrium at the given CG variables, we may still approximate VFE by means of *reweighted likelihood*.

Specifically, given locally off-equilibrium data  $\mathcal{D} = \{(\mathbf{R}; \mathbf{s}(\mathbf{R}))\}$ , we first train a model  $q_\theta$  according to the data-based objective (Eq.(6) in the main text), hence,  $q_\theta$  is a good approximation for the data distribution which is off-equilibrium. We can then implement neural importance sampling to approximate the likelihood of the equilibrium data if the reference potential energy of the data is known.

The reweighting factor  $w$  is pre-computed by an optimized  $q_\theta$  according to Eq. (S15), and a new model  $q_{\theta^*}$  is optimized according to the reweighted likelihood,

$$\begin{aligned} \nabla_{\theta^*} D_{\text{KL}}(p \parallel q_{\theta^*}) &\approx -\mathbb{E}_{\mathbf{R} \in \mathcal{D}} [w(\mathbf{R}) \nabla_{\theta^*} \log q_{\theta^*}(\mathbf{R}; \mathbf{s})] \\ w(\mathbf{R}) &\propto \exp[-\beta(\log q_{\theta}(\mathbf{R}; s(\mathbf{R})) + U(\mathbf{R}))] \end{aligned} \quad (\text{S16})$$

where  $w(\mathbf{R})$  is normalized within a mini-batch, and the resulting model  $q_{\theta^*}$  can approximate better the equilibrium distribution and lower the VFE in Eq. (10) or Eq. (S12).

#### D. Correction of VFE by FEP

Note that VFE may deviate from the ground-truth free energy by a margin if  $q_{\theta}$  is not sufficiently expressive or not well trained. Nevertheless, the accuracy of VFE can be

further improved systematically by means of FEP, yielding a corrected free energy  $F_{\text{FEP}}$  defined as follows,

$$\begin{aligned} \beta \Delta F &:= \beta(F - F_{\theta}) \\ &= -\log \mathbb{E}_{q_{\theta}} \exp[-\beta(U - U_{\theta})] \end{aligned} \quad (\text{S17})$$

$$F_{\text{FEP}} \approx F_{\theta} + \Delta F$$

where the VFE  $F_{\theta}$  is given by Eq. (10) or Eq. (S12),  $U_{\theta}$  is defined in Eq. (S13). Equation (S17) is particularly useful when  $q_{\theta}$  is optimized with respect to off-equilibrium data via the data-based objective (Eq. (6) in the main text).

---

**Algorithm S1.** Cycle Coarse Graining (CCG)

---

- 1: **Input:** Initialize generative network  $f_\theta$ , specify CG function  $\mathbf{s} = s(\mathbf{R})$ ;
  - 2: Energy model of FG structures  $U(\mathbf{R})$ ;
  - 3: Optional: paired samples  $\mathcal{D} = \{\mathbf{R}; s(\mathbf{R})\}$ .
  - 4: Set learning rates  $\alpha_\theta$  for  $\theta$ , and optimizer's hyper-parameters
  - 5: **While** convergence criteria not met, **do** ▷ begin of reconstruction
  - 7: Draw minibatch of Gaussian noise  $\{\mathbf{z}\}$
  - 8: Compute reconstructed probability  $q_\theta(\mathbf{R}; \mathbf{s})$  ▷ Eq. (7)
  - 9: Calculate gradient of energy-based objective  $\nabla_\theta \mathcal{L}_E(\theta)$  ▷ Eq. (8)
  - 10: Set data-based optimization gradient  $\nabla_\theta \mathcal{L}_D(\theta) = 0$
  - 11: **If** trained data-based objective, **do**
  - 12: Draw mini-batch of samples from  $\mathcal{D}$
  - 13: Calculate corresponding gradient  $\nabla_\theta \mathcal{L}_D(\theta)$  ▷ Eq. (6)
  - 14: **End If**
  - 15:  $\theta \leftarrow \text{Adam / SGD}(\nabla_\theta \mathcal{L}_E(\theta) + \nabla_\theta \mathcal{L}_D(\theta), \theta, \alpha_\theta)$  ▷ update generative model
  - 16: **End While** ▷ end of reconstruction
  - 17: Draw samples of Gaussian noise  $\{\mathbf{z}\}$  and specify value of CG variable  $\mathbf{s}$  ▷ begin of coarse graining
  - 18: Compute reconstructed FG structures with optimized model  $\mathbf{R} = f_\theta(\mathbf{z}; \mathbf{s})$
  - 19: Compute energy of the reconstructed FG structures  $U(\mathbf{R})$
  - 20: Obtain free energy at the given  $\mathbf{s}$ ,  $F_\theta$  ▷ Eq. (10); end of coarse graining
-

---

**Algorithm S2.** Trajectory Interpolation & Rare Event Sampling over Expensive Energy Models

---

- 1: **Input:** specify reaction coordinate  $\mathbf{s} = s(\mathbf{R})$ ;
  - 2: Oracle energy model  $U(\mathbf{R})$ ;
  - 3: Initialize surrogate energy model  $U_\phi(\mathbf{R})$ ;
  - 4: Initialize generative network  $f_\theta$ .
  - 5: Optional: paired samples  $\mathcal{D} = \{\mathbf{R}; s(\mathbf{R})\}$ .
  - 6: Set learning rates  $\alpha_\theta$  for  $\theta$ ,  $\alpha_\phi$  for  $\phi$  and optimizer's hyper-parameters
  - 7: Draw initial samples  $\{\mathbf{R}_0\}$  at  $\mathbf{s}_0$  randomly or from  $\mathcal{D}$
  - 8: **For**  $T = 1 \rightarrow N$ , **do** ▷ Active labeling for  $N$  times
  - 9: Compute labels  $\{\mathbf{R}_{T-1}\} \rightarrow \{U(\mathbf{R}_{T-1})\}$
  - 10: **For**  $t = 1 \rightarrow n_\phi$ , **do** ▷ train  $U_\phi$  for  $n_\phi$  steps
  - 11: Compute loss of surrogate model,  $\mathcal{L}(\phi) = \Delta(U_\phi(\mathbf{R}_T), U(\mathbf{R}_T))$  ▷ L1 or L2 loss
  - 12:  $\phi \leftarrow \text{Adam / SGD}(\nabla_\phi \mathcal{L}(\phi), \phi, \alpha_\phi)$  ▷ update surrogate model
  - 13: **End For**
  - 14: **For**  $t = 1 \rightarrow n_\theta$ , **do** ▷ train  $f_\theta$  for  $n_\theta$  steps
  - 15: Compute loss of generative model  $\mathcal{L}(\theta)$  ▷ Eq. (8)
  - 16:  $\theta \leftarrow \text{Adam / SGD}(\nabla_\theta \mathcal{L}(\theta), \theta, \alpha_\theta)$  ▷ update generative model
  - 17: **End For**
  - 18: Sample  $\Delta \mathbf{s}$  and update RC:  $\mathbf{s}_T = \mathbf{s}_{T-1} + \Delta \mathbf{s}$  ▷ trajectory interpolation
  - 19: Draw samples  $\{\mathbf{R}_T\}$  at  $\mathbf{s}_T$  with latest  $f_\theta$  ▷ Eq. (5)
  - 20: **End For**
-

### PART III. SUPPLEMENTAL FIGURES

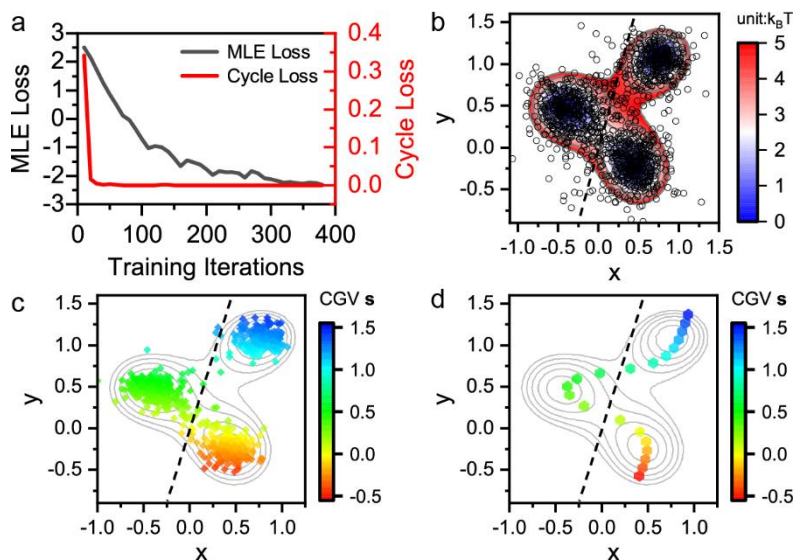


**Figure S1.** (a) The training profile of CCG, including the maximum likelihood estimation loss (MLE) or the data-based objective (black), and the consistency regularizer or cycle loss (red). (b) Off-equilibrium samples (hollow circles) from high-temperature Langevin dynamics, superimposed with the contour plot of the reference PES. (c) Factorized sampling by the CCG model trained using off-equilibrium data as shown in (b); Samples are colored according to the value of CG variable. (d) An example of interpolated trajectory, generated by feeding interpolated CG variable  $\mathbf{s}$  and fixed random noise  $\mathbf{z}$  to the CCG model  $f_\theta(\mathbf{z}; \mathbf{s})$ .

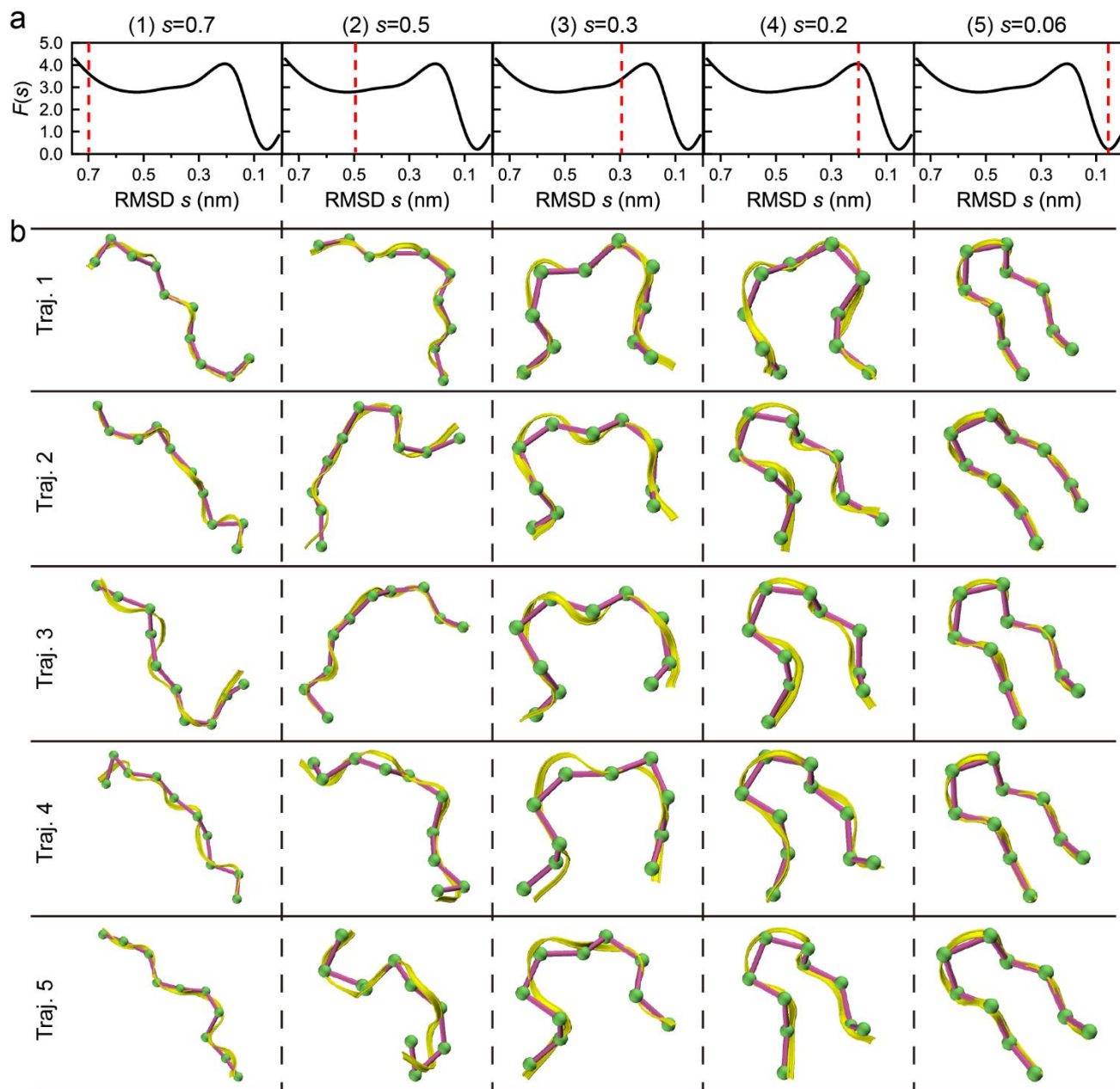


**Figure S2.** (a) The PMF along the CG variable RMSD ( $s$ ), with respect to the native structure. Column (1) to (5) correspond to five selected RMSD values at which the FGR results are inspected. (b) Five trajectories with reconstructed  $C\alpha$  structures (opaque magenta) sampled from independent random noises by trajectory interpolation at corresponding RMSD in (a); The best aligned MD structure is shown in yellow ribbons.

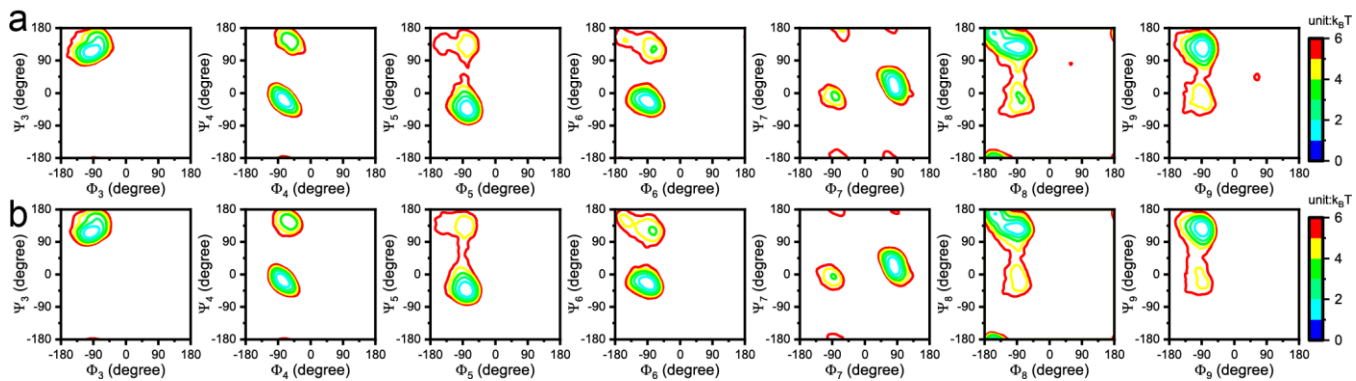


**Figure S3.** Ramachandra plots for the 3rd to 9th residues drawn for MD samples (a) and factorized sampling (b), respectively.